NUCL SCI TECH (2017) 28:119
DOI 10.1007/s41365-017-0268-x

A specialized code for operation transient analysis and its application in fluoride salt-cooled high-temperature reactors

Jian Ruan[1,2] · Bo Xu[1,2] · Ming-Hai Li[1] · Yang Yang[1] · Yang Zou[1] · Hong-Jie Xu[1]

Received: 16 July 2016 / Revised: 15 November 2016 / Accepted: 1 April 2017 / Published online: 26 July 2017
© Shanghai Institute of Applied Physics, Chinese Academy of Sciences, Chinese Nuclear Society, Science Press China and Springer Nature Singapore Pte Ltd. 2017

Abstract Fluoride salt-cooled high-temperature reactors (FHRs) include many attractive features, such as high temperature, large heat capacity, low pressure and strong inherent safety. Transient characteristics of FHR are particularly important for evaluating its operation performance. Thus, a specialized code OCFHR (operation and control analysis code of FHR) issued to study an experimental FHR's operation behaviors. The geometric modeling of OCFHR is based on one-dimensional lumped parameter method, and some simplifications are taken into consideration during simulation due to the existence of complex structures such as pebble bed, intermediate heat exchanger (IHX), air radiator (AR) and multiply channels. A point neutron kinetics model is developed, and neutron physics calculation is needed to provide some key inputs including axial power density distribution, reactivity coefficients and parameters about delayed neutron precursors. For analyzing the operational performance, five disturbed transients are simulated, involving reactivity step insertion, variations of coolant mass flow rate of primary loop and intermediate loop, adjustment of air inlet temperature and mass flow rate of air cooling system. Simulation results indicate that inherent self-stability of FHR restrains severe consequences under above transients, and some dynamic features are observed, such as large negative temperature feedbacks, remarkable thermal inertia and high response delay.

Keywords FHR · Simulation · Pebble bed · Transient analysis

This work was supported by the Strategic Priority Program of Chinese Academy of Science (XDA02010200).

✉ Yang Zou
zouyang@sinap.ac.cn

✉ Hong-Jie Xu
xuhongjie@sinap.ac.cn

[1] Shanghai Institute of Applied Physics, CAS, Jiading Campus Shanghai 201800, China

[2] University of Chinese Academy of Sciences, Beijing 100049, China

1 Introduction

Fluoride salt-cooled high-temperature reactors (FHRs), which are notable for the coated particle fuel and fluoride salt coolant, provide outstanding priority in electricity generation and process heat applications. Its concept prototype was developed by Oak Ridge National Laboratory (ORNL), Sandia National Laboratory (SNL) and the University of California at Berkeley (UCB) in 2001–2003, assimilating technical advantages of molten salt reactor (MSR) and high-temperature reactor (HTR) [1]. Chinese FHR research started in 2012 by thorium molten salt reactor (TMSR) Group of Chinese Academy of Sciences, with a conceptual design of fluoride salt-cooled high-temperature experimental reactor (FHER) [2], as shown in Fig. 1.

Molten salt and particle fuel affect greatly FHRs' transient performance. The coolant in primary loop is FLiBe ($2LiF–BeF_2$) which has low neutron absorption cross section, large heat capacity ($\sim$2400 J kg^{-1} $°C^{-1}$) and a wide range of liquid-phase temperature (450–1400 °C), providing an abundant temperature safety margin [3]. It allows FHRs to increase average power density, reduce maximum pressure tolerance of material and enhance spatial

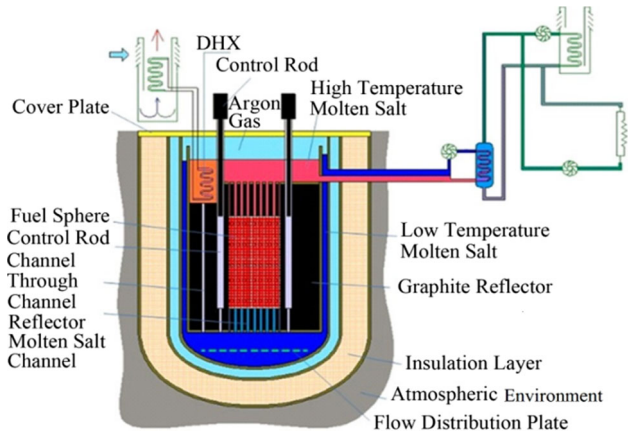

Fig. 1 (Color online) Schematic diagram of 10 MWt FHER

compactness. The fuel element consists of a fuel core (either in plate type or in spherical type) and several shielding materials (Fig. 2). The fuel core is mainly made up of tristructural-isotropic (TRISO), offering several hundred degrees safety margin comparing to rated operational temperature and leaving little possibility for fission products to leak out [4]. In this paper, spherical pebble-type fuel element is considered.

Understanding of transient performances is significant in FHR design, as the large heat capacity of salt may extend transient response time and the multilayered structure of fuel element means non-negligible temperature variation delay. Moreover, the core, pipelines and other components also restrain thermal transfer speed as it costs no less than 70 s for coolant to flow around the main loop, postponing the process of transients when disturbances occur. Therefore, it is quite necessary to study FHRs' performances under some typical operation distur bances.

Analysis of transient operation has been done experimentally or theoretically. Chen used MATLAB platform to analyze the transient performances of an FHR coupled with a helium Brayton power cycle [5]. Li simulated some kinds of disturbed transients' influence on TMSR-SF1, with the RELAP5 codes, to summarize its characteristics [6]. Lv developed a computer code to evaluate the direct reactor auxiliary cooling system (DRACS) [7]. Ablay used a modeling and control approach to study the power conversion performance of advanced nuclear plants with gas turbines [8].

In this paper, the OCFHR (operation and control analysis code of FHR) is introduced in detail, including the equations, simplifications and equivalences of complex structures, and verification of calculation models. Five disturbed transients are simulated, involving reactivity step insertion, and changes in mass flow rate of coolant of three loops and in air inlet temperature of air cooling system. The simulation results of the entire FHR system are compared with those from RELAP5 code. Additional work will be performed to study operation control logic and power conversion [9].

2 Method

2.1 Algorithm

CFHR is implemented by fourth-order Runge–Kutta (R–K) method for numerical solution of differential equations. This algorithm is an explicit numerical difference scheme, and it can construct arbitrary high-order calculation method [10]. Besides, Gear algorithm, a variable step length algorithm, is programed in comparison with R–K method on computation speed and accuracy.

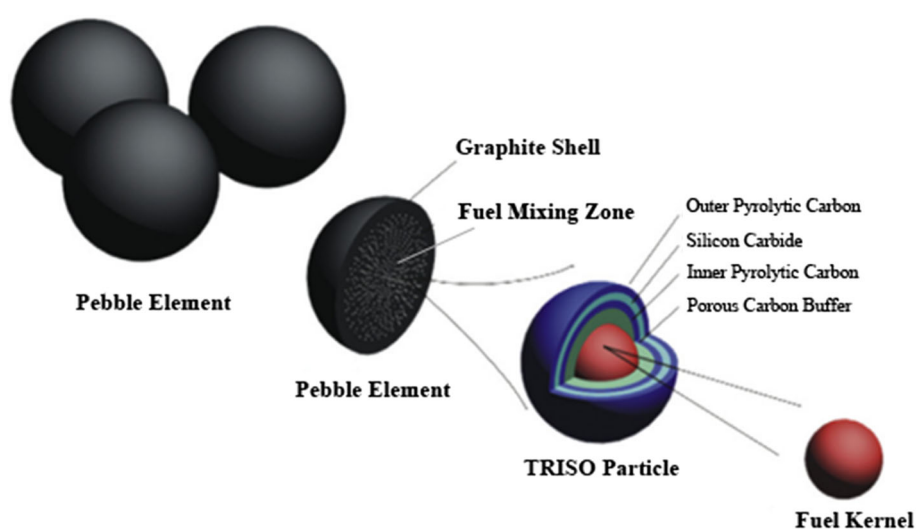

Fig. 2 (Color online) Schematic diagram of pebble element

2.2 Simplification

The FHER system consists of the pebble bed, cavities, pipes, pumps, heat exchangers, load etc. The simplification of FHR system in OCFHR is based on lumped parameter method, which axially divides the object structure into several independent nodes, each representing segmental geometrical and physical parameters. Differential equations for material properties and heat transfer, and conservation equations, are developed within a node. Every component model in OCFHR is labeled by a series of numbers, each denoting a node. When an additional structure is added in, so will the label number be inserted into the array. Hence, the whole system is simplified under this modularization thinking, which brings in significant progress in modeling speed [11]. Figure 3 shows the node diagram. The primary coolant heated from the core flows along the upper cavity and the hot leg to the inlet of IHX. Then, the cooled salt reaches to the inlet of downcomer and lower cavity, eventually returns back to the core. Positions E and D are inlet and outlet of IHX cooling side, while F and G are inlet and outlet of SHX heating side. Figure 4 represents simplifications of the pebble bed. Relevant parameters of FHER are given in Table 1.

It is impossible to model the complicated bed structure without compromise because the core contains more than ten thousand pebbles and each pebble has thousands of TRISO particles. In OCFHR, the bed is divided into two areas: cylindrical graphite shells and cylindrical fuel mixing zone. The former structure strengthens the pebble, while the latter contains TRISO particles and graphite moderator. Some parameters are acquired from neutron physics program such as temperature reactivity coefficients, decay constants and portions of neutron precursors. Heat transfer calculation of the core uses the mature porous medium Wakao correlation due to the impractical calculation of heat transfer between pebble bed and salt coolant. For heat transfer calculation between the bed and coolant, the Wakao correlation is often used [12].

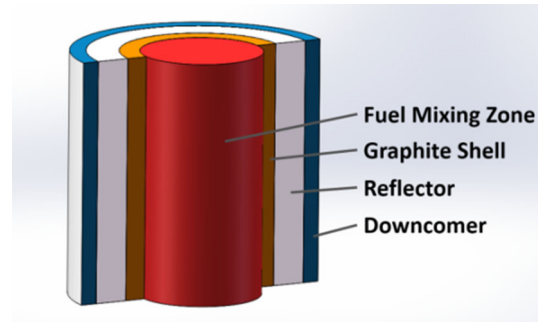

Fig. 4 (Color online) Simplifications of pebble bed

$$Nu = 2.0 + 1.1 Re_{\mathrm{D}}^{0.6} Pr^{1/3}, \quad (1)$$

where Nu is the Nusselt number, Re is the Reynolds number, Pr is the Prandtl number, and D is the equivalent

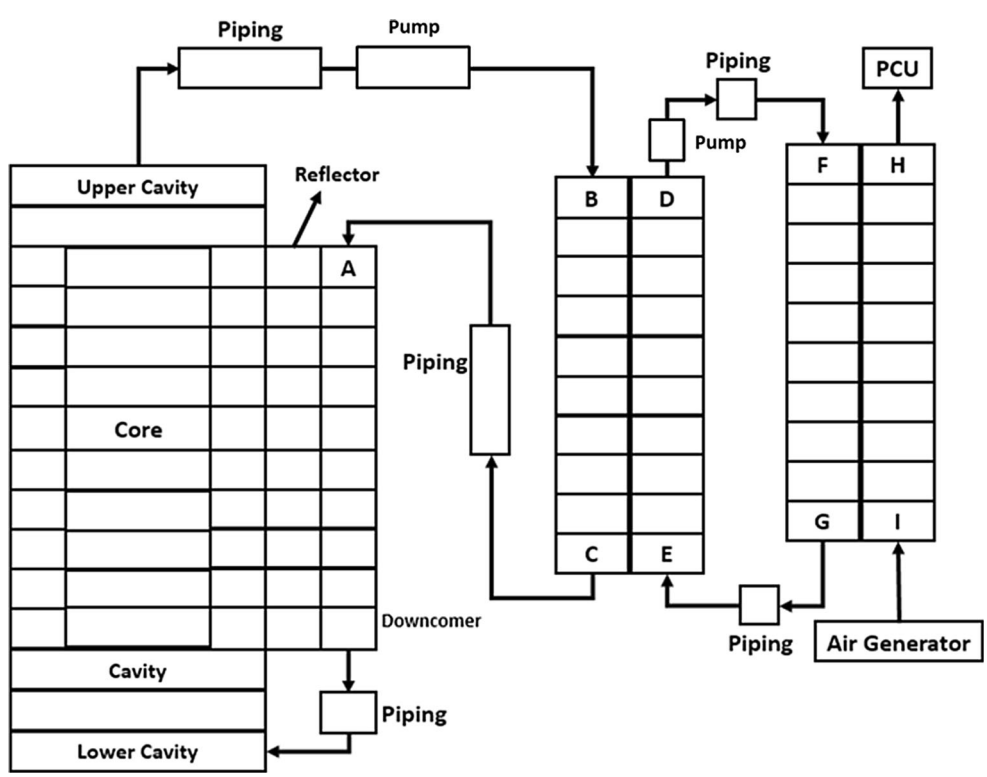

Fig. 3 Node diagram of FHER

Table 1 FHER geometric structure parameters

Parameters	Values
Fuel pebble diameter (cm)	6.00
Fuel pebble number	10,855
Graphite shell thickness (cm)	1.00
TRISO particles in one pebble	10,000
Diameters of TRISO shells (outwards) (μm)	250/430/500/580
Active zone cylinder diameter (m)	1.35
Active zone cylinder height (m)	1.30
Active zone volume (m^3)	2.76
Upper reflector volume (m^3)	0.72
Lower reflector volume (m^3)	0.63
Upper plenum volume (m^3)	0.64
Lower plenum volume (m^3)	0.27
Diameter of pipe (m)	0.126
Length of hot leg (m)	10.0
Length of cold leg (m)	10.0
Reflector diameter(m)	2.85
Reflector height (m)	3.00
Total length of secondary loop (m)	20.0
FLiBe volume in IHX (m^3)	0.64
FLiNaK volume in IHX (m^3)	1.35
FLiNaK volume in SHX (m^3)	0.70

diameter. Equation (1) is applicable for $15 < Re < 8500$ [13].

Before calculation, some assumptions are adopted as follows:

(1) The whole system is under perfect thermal insulation, and all heat losses to the environment are neglected.
(2) Consider the heat transfer between pebble and salt is merely heat convection.
(3) Neglect the deformation of bed geometry caused by vibration and flow of fluid.
(4) Consider that average temperature of the fuel mixing zone equals to the surface temperature of fuel mixing zone in a pebble which is at the center of node, while the node occupies the highest power distribution factor.
(5) The heat fluxes of TRISO particles within same pebble are same.

2.3 Mathematic model

The mass conservation in one fluid node conforms to that mass flow rate at the outlet equals to that at the inlet. The second item in Eq. (1) can be rewritten as one direction due to that the model is one dimensional.

$$\frac{\partial \rho}{\partial t} + \nabla \cdot (\rho V) = 0, \tag{2}$$

$$\frac{\partial \rho}{\partial t} + \frac{\partial \rho u}{\partial x} = 0, \tag{3}$$

where V is velocity vector, ρ is the density of coolant (kg m^{-3}), and u is the average flow rate of coolant on x-dimension (m s^{-1}).

The coolant is driven by pump, which offers the pressure head to compensate the friction pressure drop, form pressure drop and gravitation pressure drop. The flow rate of coolant is determined by the difference between the pump pressure head and resistance pressure drop,

$$\frac{\partial W}{\partial t} + \frac{\partial}{\partial x}\left(\frac{W^2}{\rho A}\right) + \frac{fW^2}{2\rho DA} + \frac{KW^2}{2\rho A} = \frac{\partial P}{\partial x}, \tag{4}$$

where W is mass flow rate of coolant (kg s^{-1}), f is the factor of friction pressure drop, K is the factor of form pressure drop, and P is pressure head of pump. Therefore, the integral form of Eq. (4) can be written as:

$$\sum_{i=1}^{m}\left(\frac{L}{A}\right)_i \frac{\mathrm{d}W}{\mathrm{d}t} + \Delta P_\mathrm{f} + \Delta P_\mathrm{K} + \Delta P = 0, \tag{5}$$

where m is the number of pipes or other sections, ΔP_f is the friction pressure drop, and ΔP_K is the form pressure drop.

For a TRISO particle, thermal conductivity formula is adopted to calculate temperature gradient from its outer pyrolytic carbon shell to fuel particle. Based on the simplifications and assumptions above, the temperature of center fuel zone in the hottest TRISO can be calculated as:

$$c_\mathrm{pf} m_\mathrm{f} \frac{\partial T_\mathrm{f}}{\partial t} = -\frac{(T_\mathrm{f} - T_\mathrm{g})}{R_\mathrm{fg}} + P_\mathrm{f} F. \tag{6}$$

The heat transfer form in pebble graphite shell can be calculated by:

$$c_\mathrm{pg} m_\mathrm{g} \frac{\partial T_\mathrm{g}}{\partial t} = \frac{(T_\mathrm{f} - T_\mathrm{g})}{R_\mathrm{fg}} - (T_\mathrm{g} - T_\mathrm{s}) h_\mathrm{gs} A_\mathrm{gs} - \varepsilon_\mathrm{g} A_\mathrm{ge} \sigma \left(T_\mathrm{g}^4 - T_\mathrm{ge}^4\right), \tag{7}$$

where P_f is the reactor power (W); F is the power axial distribution factor; $c_\mathrm{pf} m_\mathrm{f}$ is the specific heat capacity of the fuel mixing zone (J/°C); T_f is the fuel mixing zone temperature (°C); T_s is the primary coolant temperature (°C); T_ge is the graphite reflector temperature (°C); T_g is the external graphite temperature in a node (°C); $c_\mathrm{pg} m_\mathrm{g}$ is the specific heat capacity of the node (J/°C); h_gs is equivalent heat transfer coefficient between graphite and molten salt (W m^{-2} °C^{-1}); A_gs is the heat transfer area between graphite zone and external salt; A_ge is the radiation area between graphite zone and graphite reflector; ε_g is the effective radiation coefficient between external graphite

zone and reflector; and R_{fg} is the thermal resistance between internal fuel mixing zone and external graphite. The subscripts f, g, s and ge denote the mixing zone, graphite shell, primary coolant and reflector, respectively. Figure 5 shows the heat transfer process in the core.

In a primary coolant node of core,

$$c_{ps}m_s\frac{\partial T_s}{\partial t} = (T_g - T_s)h_{gs}A_{gs} - (T_s - T_{ge})h_{ge}A_{ge} - c_{ps}\dot{m}_s(T_{out} - T_{in}), \quad (8)$$

where m_s is the coolant mass in one node (kg); c_{ps} is the coolant specific heat (J kg^{-1} °C^{-1}); $\dot{m}_s$ is the coolant mass flow rate (kg s^{-1}); and T_{out} and T_{in} are molten salt outlet and inlet temperatures, respectively, in one node.

In a graphite reflector node,

$$c_{pge}m_{ge}\frac{\partial T_{ge}}{\partial t} = \varepsilon_{ge}A_{ge}\sigma\left(T_g^4 - T_{ge}^4\right) + (T_s - T_{ge})h_{ge}A_{ge} - (T_{ge} - T_{sd})h_{gd}A_{gd}, \quad (9)$$

where c_{pge} is the graphite specific heat (J kg^{-1} °C^{-1}); m_{ge} is the graphite reflector mass of one node; T_{ge} is the graphite temperature in one node (°C); T_{sd} is the temperature of salt in one node of downcomer (°C); h_{ge} is the equivalent heat transfer coefficient between salt and reflector (W m^{-2} °C^{-1}); h_{gd} is the equivalent heat transfer coefficient between salt in the downcomer and reflector (W m^{-2} °C^{-1}); and A_{gd} is the effective heat transfer area.

In a coolant node of downcomer,

$$c_{ps}m_{sd}\frac{\partial T_{sd}}{\partial t} = (T_{ge} - T_{sd})h_{gd}A_{gd} - c_{ps}\dot{m}_s(T_{out} - T_{in}) - \dot{P}_0, \quad (10)$$

where m_{sd} is the coolant mass in one node (kg); $\dot{m}_s$ is the coolant mass flow rate (kg s^{-1}); and $\dot{P}_0$ is the heat release rate of the reactor vessel, which is set as zero under the first assumption.

For the pressure drop in the core, the Ergun equation, which is suitable for porous medium, can be used [14]:

$$\frac{\Delta P_c}{L} = -\frac{150\mu}{D_p^2}\frac{(1-\varepsilon)^2}{\varepsilon^3}u_i - \frac{1.75\rho}{D_p}\frac{(1-\varepsilon)}{\varepsilon^3}|u|u_i, \quad (11)$$

where ΔP_C is the core pressure drop, ε is the volume fraction, μ is the viscosity, D_p is the pebble diameter, and L is the height of pebble bed. Nuclear power calculation is based on the fifteen-group point kinetic equations:

$$\frac{dn(t)}{dt} = \frac{\rho(t) - \beta}{l}n(t) + \sum_{i=1}^{15}\lambda_i C_i(t)\frac{dC_i(t)}{dt} = \frac{\beta_i}{l}n(t) - \lambda_i C_i(t), \quad (12)$$

where n is the neutron density (n m^{-3}); C is the concentration of neutron precursor; β is the total delayed neutron fraction; β_i is the ith delayed neutron fraction; λ is the decay constant (s^{-1}); and l is the mean neutron generation time (s). β, λ and l are gained from neutron physics calculation, while the external source of neutron is neglected. Among the 15 delayed neutron precursor groups, nine groups are added in due to the photo-neutron emission. This enlarges neutron lifetime and increases the effects of delayed neutrons [15].

Negative reactivity feedback model contains the effects of fuel, coolant, moderator and reflector. Fuel reactivity coefficient is negative due to the Doppler effect, and that of primary coolant also shows negative due to its neutron property. Besides, the control rod effect is an important way to control reactivity in most FHR designs.

$$\rho(t) = \rho_0 + \rho_{rd} + \alpha_{fg}\Delta\bar{T}_{fg} + \alpha_s\Delta\bar{T}_s + \alpha_{ge}\Delta\bar{T}_{ge}, \quad (13)$$

where ρ_0 is the initial reactivity; ρ_{rd} is the control rod reactivity; α_{fg} is the mixing zone reactivity coefficient; α_S is the primary coolant reactivity coefficient; α_{ge} is the graphite reflector reactivity coefficient; and $\boldsymbol{\Delta\bar{T}_{fg}}$, $\boldsymbol{\Delta\bar{T}_s}$ and $\boldsymbol{\Delta\bar{T}_{ge}}$ are mean temperature change values (°C) of the mixing zone, primary coolant and reflector, respectively.

The IHX model is the smooth shell- and tube-type heat exchanger (STHX).Compared with spirally fluted tube, its

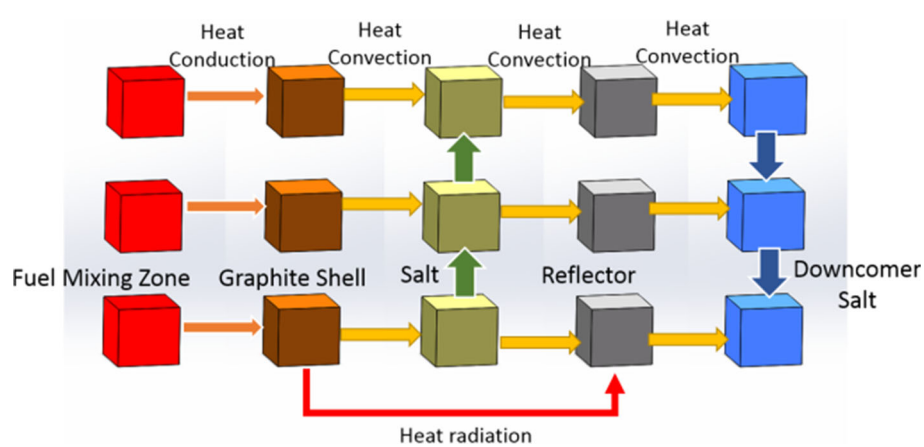

Fig. 5 (Color online) Heat transfer process in the core

pressure drop and fabricating cost is lower, while heat transfer efficiency is weakened by half. Figure 6 shows a cross section of the IHX. The IHX operates under a FLiBe-to-FLiNaK environment, while the primary coolant flows on the tube side and the secondary coolant flows on the shell side. Detailed parameters of IHX are shown in Table 2.

For the tube side,

$$c_{ps} m_{ep} \frac{\partial T_{ep}}{\partial t} = -(T_{ep} - T_{ed}) h_{ep} A_{ep} + c_{ps} \dot{m}_s (T_{inep} - T_{outep}), \tag{14}$$

where c_{ps} is the internal salt specific heat (J kg^{-1} °C^{-1}); m_{ep} is internal coolant mass in a node (kg); T_{ep} is internal coolant temperature (°C); T_{ed} is the intermediate wall temperature (°C); h_{ep} is the equivalent heat transfer coefficient between salt in the tube and wall (W m^{-2} °C^{-1}); A_p is the effective heat transfer area; and T_{inep} and T_{outep} are the tube side coolant temperatures at the tube inlet and outlet, respectively.

For the shell side,

$$c_{ss} m_{es} \frac{\partial T_{es}}{\partial t} = (T_{ed} - T_{es}) h_{es} A_{es} + c_{ss} \dot{m}_{ss} (T_{inss} - T_{outss}), \tag{15}$$

where c_{ss} is the external salt specific heat (J kg^{-1} °C^{-1}); m_{es} is external coolant mass in a node (kg); T_{es} is coolant temperature (°C); h_{es} is the equivalent heat transfer coefficient between salt in the tube and wall (W m^{-2} °C^{-1}); A_{es} is the effective heat transfer area; and T_{inss} and T_{outss} are the shell side coolant temperatures at the shell inlet and outlet, respectively.

The heat transfer between tube side and shell side of IHX and SHX is heat convection. Based on the simplification of heat exchanger, pipe bundles are approximated to a pipe of the same length, equivalent diameter and heat exchanger area. The correlations used in this study are listed as follows [16].

For the tube side

$$Nu = 0.027 Re^{0.8} Pr^{1/3} \left(\frac{\mu}{\mu_w} \right)^{0.14}, \tag{16}$$

For the shell side

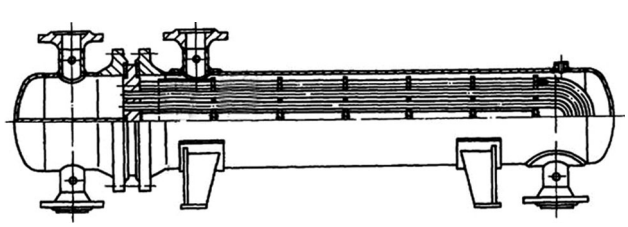

Fig. 6 Schematic diagram of IHX model

Table 2 IHX and SHX parameters

Parameters	Values
IHX primary side inlet temperature (°C)	700.0
IHX primary side outlet temperature (°C)	672.0
IHX secondary side inlet temperature (°C)	610.0
IHX secondary side outlet temperature (°C)	630.0
IHX tube number	1210
IHX tube thickness (mm)	1.65.0
IHX effective tube length (m)	2.8.0
IHX equivalent heat transfer coefficient (W m^{-2} K^{-1})	1200.0
SHX secondary side inlet temperature (°C)	40.0
SHX secondary side outlet temperature (°C)	151.0
SHX tube number	2016
SHX tube thickness (mm)	1.7
SHX effective tube length (m)	3.3
SHX equivalent heat transfer coefficient (W m^{-2} K^{-1})	108.0

$$Nu = 0.3 + \frac{0.62 Re^{0.5} Pr^{1/3}}{\left[1 + (0.4/Pr)^{2/3}\right]^{1/4}} \left[1 + \left(\frac{Re}{28200} \right)^{5/8} \right]^{0.8}, \tag{17}$$

where μ and μ_w are coolant viscosities calculated by coolant temperature and wall temperature, respectively.

Currently, FHER adopts an air fan as the load. In OCFHR, the AR model also uses an air fan as the heat sink for the hot secondary coolant flowing in the SHX from IHX cold side outlet. The type of SHX model is similar to IHX, with FLiNaK flowing in the tube and the air flowing in the shell. The inlet air is at 40°C under normal conditions.

3 Results and discussion

3.1 Steady-state operation

Only when the model reaches its rated steady state, will disturbed transients be introduced. The steady-state operation parameters, node temperatures and delayed neutron group parameters are given in Tables 3, 4 and 5, respectively.

3.2 Model solver verification

OCFHR employs a 15-group point kinetic model to calculate nuclear power. To verify the model's reliability, the isolated point reactor model is compared with that based on Gear and numerical differentiation formulas (NDFs) algorithms by inserting a negative step reactivity of −100 pcm. Also, a single-group point kinetic model based

Table 3 FHER steady-state operating parameters

Parameters	Values
Total thermal power (MW)	10.0
Primary coolant inlet temperature (°C)	672.0
Primary coolant outlet temperature (°C)	700.0
Primary coolant mass flow rate (kg s^{-1})	150.0
Pressure drop of pebble bed (Pa)	2200
Fuel mixing zone TCR (pcm $°C^{-1}$)	−5.69
Salt TCR (pcm $°C^{-1}$)	−2.27
Graphite TCR (pcm $°C^{-1}$)	0.74
Secondary coolant mass flow rate (kg s^{-1})	260.0
Secondary coolant inlet temperature (°C)	610.0
Secondary coolant outlet temperature (°C)	630.0
Air fan mass flow rate (kg s^{-1})	51.0

TCR temperature coefficient of reactivity

Table 4 Node temperature (°C)

Inlet of downcomer	672
Inlet of IHX hot side	700
Outlet of IHX hot side	672
Outlet of IHX cold side	630
Inlet of IHX cold side	610
Inlet of SHX hot side	630
Outlet of SHX hot side	610
Outlet of SHX cold side	227
Inlet of SHX cold side	40

Table 5 Delayed neutron group parameters

No.	β	λ
1	2.11E–4	1.24E–2
2	1.395E–3	3.05E–2
3	1.25E–3	1.11E–1
4	2.514E–3	3.01E–1
5	7.35E–4	1.14
6	2.684E–4	3.02
7	5.512E–7	6.24E–7
8	3.67E–7	2.48E–6
9	2.514E–6	1.59E–5
10	3.094E–5	6.2E–5
11	3.481E–6	2.67E–4
12	3.559E–5	7.42E–4
13	1.789E–5	3.6E–3
14	3.54E–5	8.85E–3
15	2.0E–5	2.26E–2

on the R–K method is compared with the analytical solution by inserting a positive step reactivity of 250 pcm to test its accuracy. The time step is 0.01 s, and the results are shown in Fig. 7.

In Fig. 7a, the numerical solution of OCFHR agrees well with that of Gear and NDFs. Although different algorithms have different error handling methods which may cause small error, these results prove that R–K method is viable. From Fig. 7b, R–K numerical solution matches well with single-group analytical solution and the truncation error can be neglected [17].

The thermal hydraulic calculation is based on lumped parameter method. A simple case (Fig. 8; Table 6) is simulated and compared with RELAP5: FLiBe salt flows through a heated pipe ora cooled pipe. The start temperature of the salt and walls is 600 °C. Then, it begins to change as the heating power and cooling power is added to pipe walls.

Figure 9 shows that the temperatures of walls near the heater and the cooler response quickly, while the temperature of cold salt drops at first. Nodes 1 and 2 are the first and last wall node right next to the fluid, respectively. The maximum wall temperature difference between OCFHR and RELAP5 is 1.1°C with a calculation deviation of 0.11%, caused probably by different calculation methods. The errors of salt and wall temperatures in Fig. 10 prove the validity of thermal hydraulic calculation method and its reliability to simulate transient behavior of the FHER.

3.3 Transient simulation

OCFHR is programed for simulating and analyzing normal operation transient behavior of FHR. Before simulation, the types of operation transient should be clarified. The disturbances simulated are based on the possibilities of happening during normal operation. According to experimental and engineering experience, four typical transients are listed in Table 7.

The dynamic model must reach a rated steady state in the first place. Then, the disturbed transients shown above will be introduced into the system. Considering the reactivity inserted and mass flow rate changes in the transients are of larger impacts than other disturbances, and all safety control modules are forbidden during the simulations, this work can help to figure out the operation stability and security of FHER.

3.3.1 100 pcm positive reactivity step insertion

A reactivity step insertion accident may happen during normal operation, if control rod is extracted or inserted by accident, or even by a blackout. When reactivity is step-inserted into the reactor, the nuclear power may fluctuate strongly in a short time.

Figure 11a shows that after a step insertion of positive reactivity, the reactor power reaches the maximum power at about 20 s before it is overwhelmed by the negative

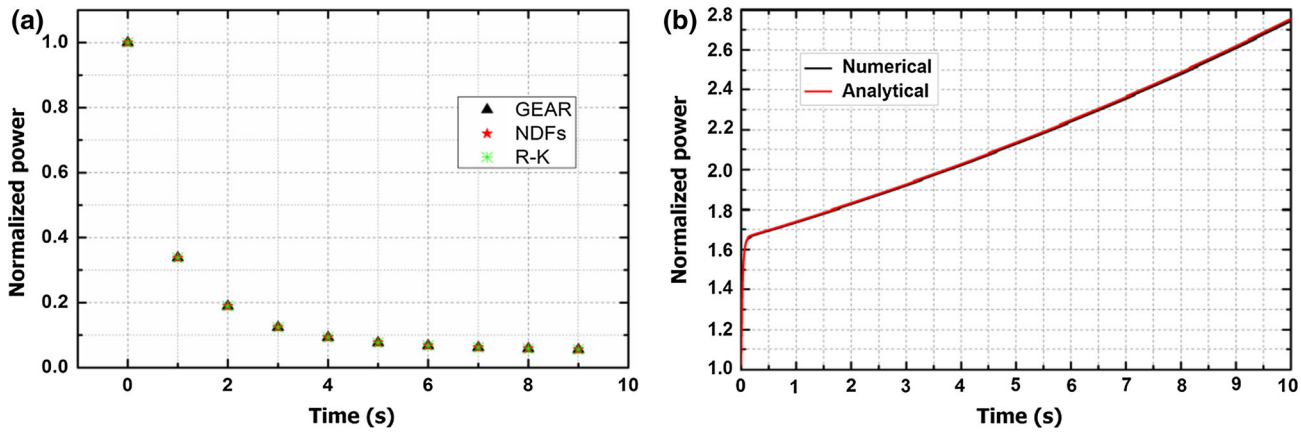

Fig. 7 Reactor power level behavior following negative (**a**) and positive (**b**) step reactivity insertion based on different algorithm models

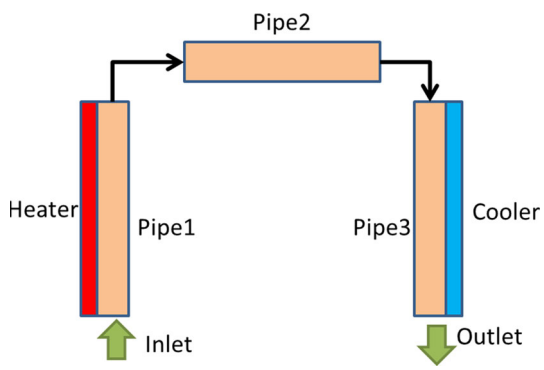

Fig. 8 (Color online) Loop structure of the case

Table 6 Parameters of case

Parameters	Values
Pipe length (m)	50
Pipe thickness (m)	0.05
Pipe cross-sectional area (m^2)	1.0
Pipe diameter (m)	1.128
Salt inlet temperature (°C)	600
Mass flow rate (kg s^{-1})	100
Heater power density (W m^{-2})	50,000
Cooler power density (W m^{-2})	−50,000
Radial node number of heater and cooler	10
Axial node number of heater and cooler	20
Calculation time range (s)	10,000

temperature reactivity feedback mainly produced from the fuel and coolant. At about 800 s, the power reaches a steady state of 10.36 MW, being about 0.36 MW higher than the origin. Figure 11b shows the coolant temperature change after the reactivity step insertion. Following the rising nuclear power, the temperature of the pebble center increases quickly to the peak temperature of 955 °C, which is much less than the design critical temperature. After nearly 65 s, the coolant temperature at core inlet begins to increase, while the interval is roughly the same as the circulation time of primary loop. The secondary coolant temperature at IHX outlet begins to increase at about 22 s and the coolant at IHX inlet increases at 30 s, which is also similar to the circulation time of secondary loop. After nearly 600 s, the temperatures of system stabilize at new operating points. The average temperatures of fuel mixing zone and graphite increase by 14 and 12 °C. The temperatures of primary loop at IHX inlet and outlet increase by about 10 and 11 °C, while those in the secondary loop are 12.2 and 12.6 °C, respectively.

3.3.2 10% of primary coolant mass flow rate step increases

This accident happens due to the shifting of pump operation state or a breakdown, and 10% increase of mass flow rate is relatively large for normal operation. This disturbance can decrease fuel temperature for a time, and then fuel temperature increases as positive feedback is inserted. Figure 12a shows that when the primary coolant mass flow rate rises due to incorrect operation of the pump, the heat exchange in core becomes intensive. Positive reactivity is added into the core due to the negative reactivity feedback of fuel and coolant. After that, negative reactivity is induced back to counteract the previous effect as temperature continues to go up. At about 800 s, a stable value is reached and the power is nearly 0.1 MW higher than its initial value. Figure 12b shows fluid temperature curve in this process. It is observed that the primary coolant temperature decreases first due to the extra flow rate, then increases going after the rising power. However, the temperature of fluid and fuel merely changes during the case. Still, after nearly 300 s, all temperatures stabilize apparently. The average temperatures of fuel zone and graphite shell decrease by only 0.1 and 0.6 °C. The core inlet temperature

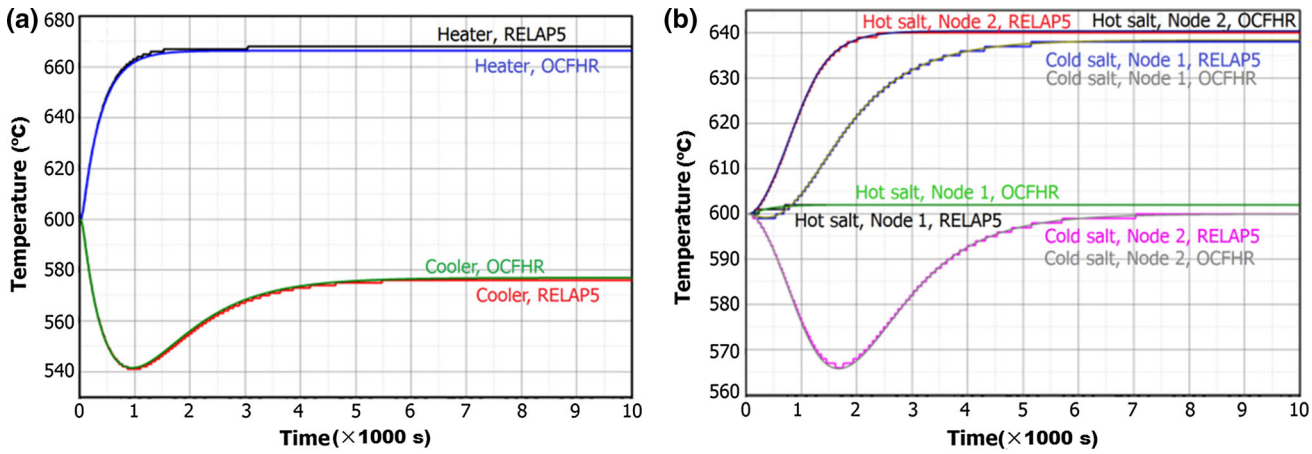

Fig. 9 (Color online) Simulation results of temperatures of (**a**) the heater and cooler and (**b**) the salt, for the case shown in Fig. 8 and Table 6

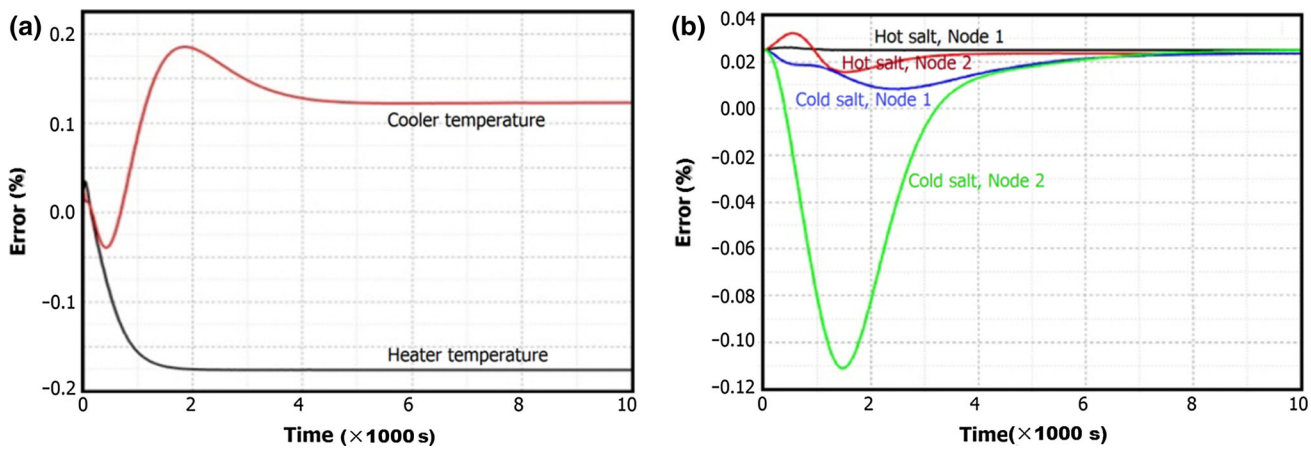

Fig. 10 (Color online) Relative temperature errors of (**a**) the heater and cooler and (**b**) the salts

Table 7 Transients and disturbances under normal operation

Title	Reason	Values
Reactivity step insertion	Maloperation of control rod	±100 (pcm)
Coolant mass flow rate step change	Maloperation of pump/short electricity cut of pump	±(0–10%)
Air inlet temperature change	Ambient temperature change	±10 (°C)
Air inlet flow rate change	Misoperation of air radiator	±(0–20%)

ascends by 2 °C, and the core outlet temperature decreases by 0.5 °C. Besides, the secondary coolant temperature increases 3.3 °C at IHX inlet and 3.5 °C at IHX outlet, approximately. It can be concluded that the change of fluid flow rate matters little on the fluid temperature.

3.3.3 10% of secondary coolant mass flow rate step increases

As the secondary coolant mass flow rate changes, the nuclear power needs a relatively longer time to response. This is due to the large heat transfer delay of the system and the large thermal inertia of the molten salt. Figure 13a shows that at about 40 s, the power begins to response according to the positive reactivity inserted by fuel and coolant temperature changes. At nearly 600 s, the power becomes stable at 10.046 MW. From Fig. 13b, at the start of this simulation, the temperature of secondary coolant changes quickly but not apparently, and the primary coolant temperature varies inconspicuously. FLiBe temperatures at core inlet and outlet decrease by 0.34 and 0.4 °C, respectively. The FLiNaK temperatures at IHX inlet and outlet increase by 2.4 and 0.6 °C, respectively. The characteristics of molten salt make the change of mass

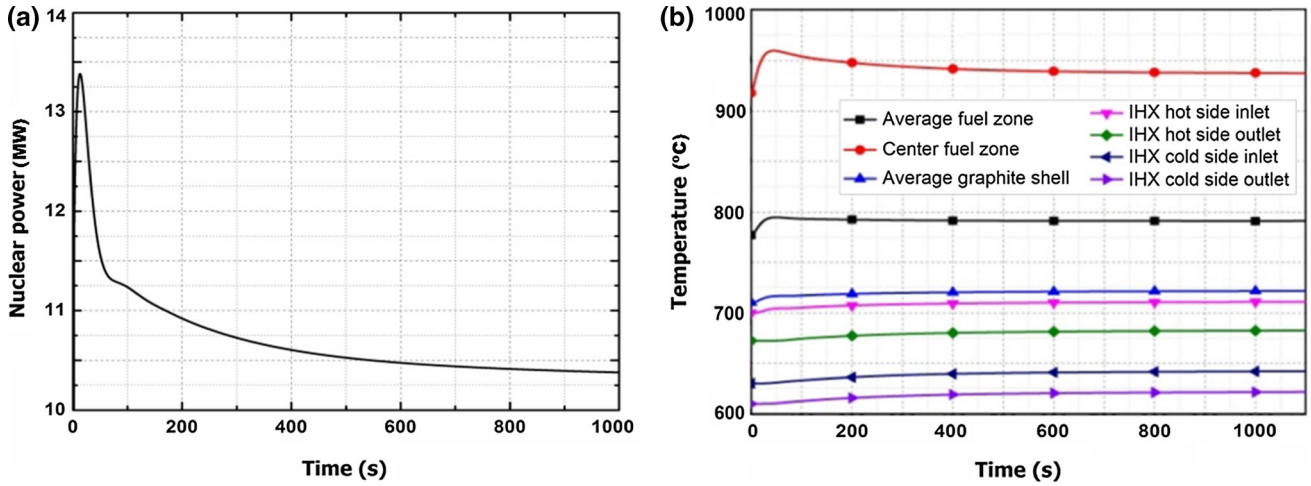

Fig. 11 (Color online) Reactor power evolution (**a**) and coolant temperatures (**b**) after reactivity step insertion

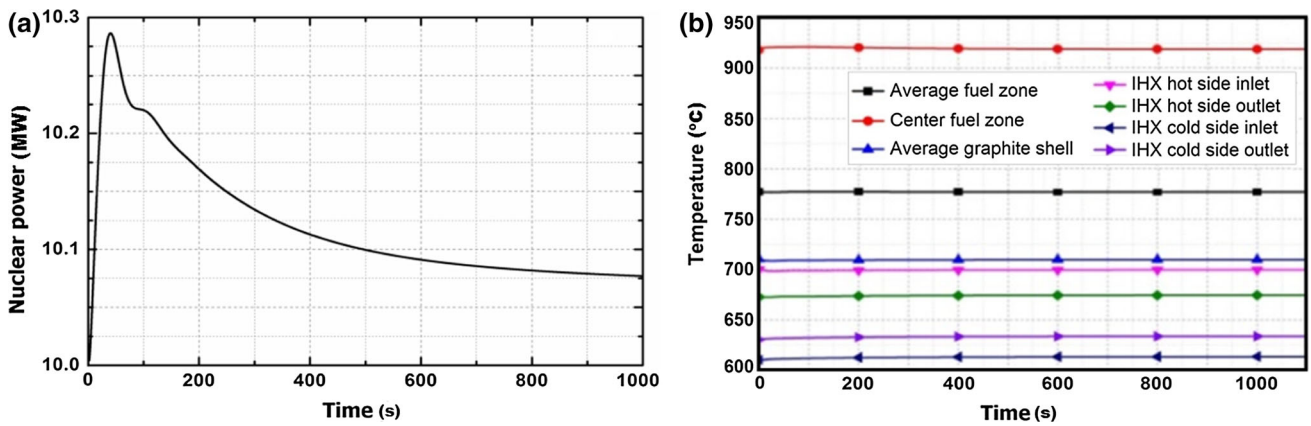

Fig. 12 (Color online) Reactor power evolution (**a**) and coolant temperatures (**b**) after mass flow change

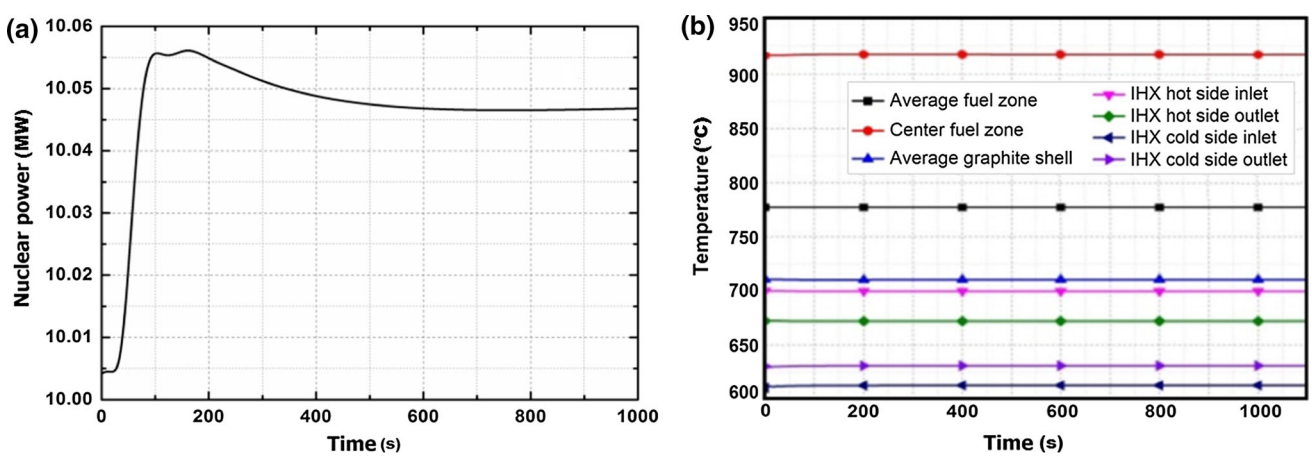

Fig. 13 (Color online) Reactor power evolution (**a**) and coolant temperatures (**b**) after mass flow change

flow have little influence on the nuclear power and primary coolant operation condition. When this incorrect operation occurs, FHR can deal well with the case without any other intervening measures.

3.3.4 20% of air mass flow rate step increases

Reactor's load cannot be shifted synchronously with the nuclear power, and sometimes step change may occur

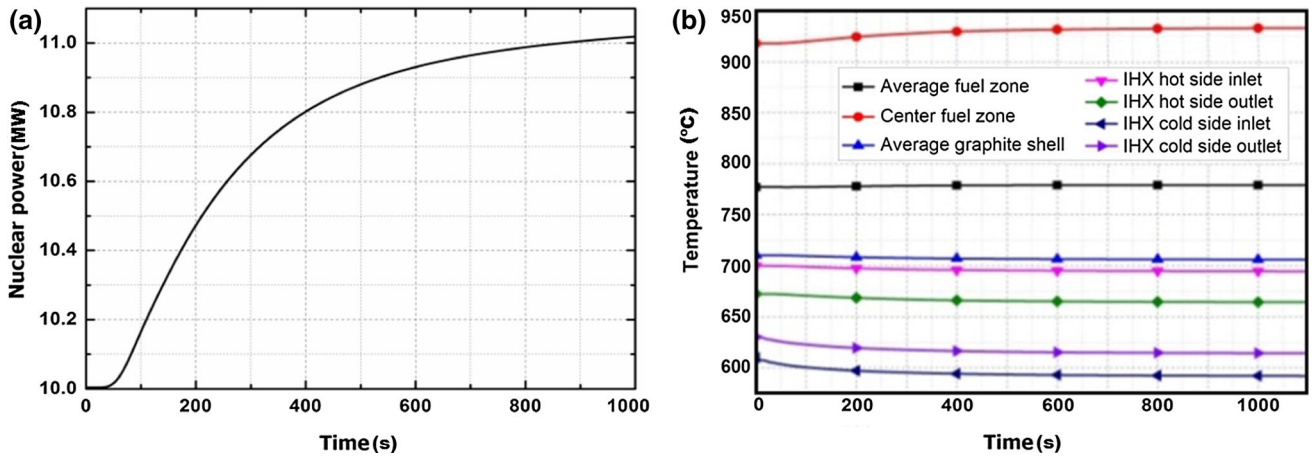

Fig. 14 (Color online) Reactor power evolution (**a**) and coolant temperature (**b**) after load change

in its operation point. This case is used in the load following operation mode. Figure 14a shows that the power increases slowly from 50 s and reaches steady state at about 1000 s. The maximum of power is about 11.05 MW. Figure 14b shows that temperature of the average fuel zone increases by 2 °C, while the shell average temperature decreases by 4.5 °C. The temperatures of primary coolant in core inlet and outlet begin to decrease at nearly 40 s and reach to a stable value at about 600 s, which are about 8 °C lower and 6 °C lower than the initial values, respectively. On the contrary, the secondary coolant temperature responds quickly and it reaches stable state at about 600 s. The secondary coolant temperatures in IHX inlet and outlet decrease by 18.3 and 16 °C, respectively. From Fig. 14, we can know that the nuclear power is connected to the fan's flow rate, but not a positive correlation relationship, since the fan's air temperature changes with the nuclear power.

3.3.5 10 °C of air generator inlet temperature increases

Due to the use of fan as a PCU, a new disturbance of air inlet temperature is inserted into FHER system if no equipment exists to control the inlet air temperature, and temperature change of 10 °C is large enough for surroundings. We assume that the air inlet temperature increases from 40 to 50 °C in 10 min to research the transient variation of the FHER. In Fig. 15a, the nuclear power decreases at about 50 s and stabilizes at its minimum value of 9.82 MW after 1500 s. This is because the increasing air inlet temperature can impede heat transfer. The temperature of secondary coolant increases slowly, and the temperatures of fuel, shell and primary coolant do not change apparently. Both of the coolant temperatures become stable after about 800 s. Besides, the temperature of fuel zone decreases by 0.5 °C and the temperature of graphite shell increases by 1 °C. The temperatures of

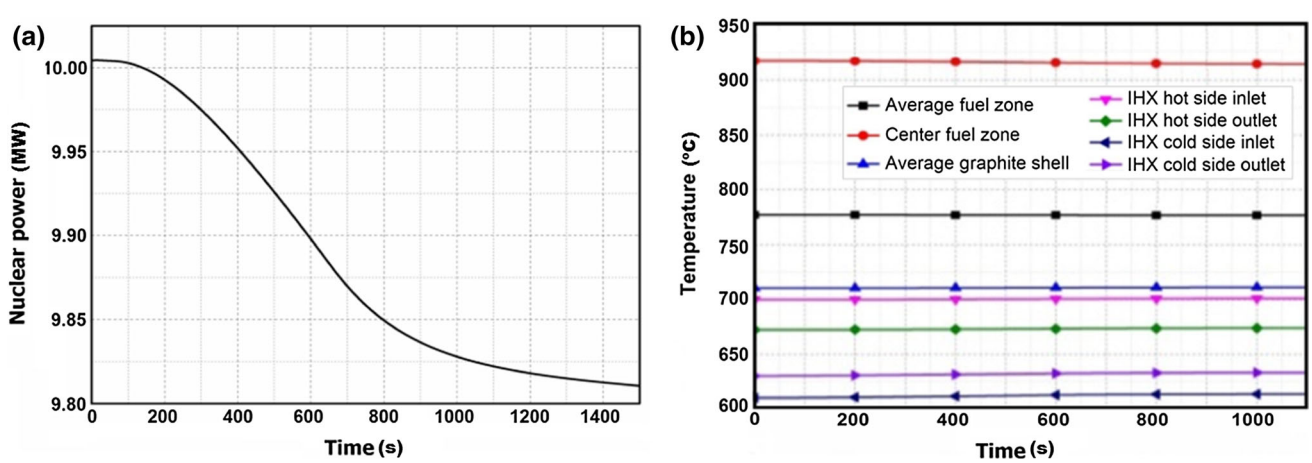

Fig. 15 (Color online) Reactor power evolution (**a**) and coolant temperatures (**b**) after air temperature change

Table 8 Steady-state parameters of FHER after inserting transient disturbance

Parameters	0	1	2	3	4	5
Power (MW)	10	10.36	10.07	10.05	10.96	9.81
Max deviation from initial Power (MW)	–	+3.76	+0.28	+0.06	+0.96	−0.19
Fuel zone average temperature (°C)	777.1	791.2	777.0	777.2	779.0	776.7
Max deviation from initial fuel zone average temperature (°C)	–	+14.1	−0.1	+0.12	+1.9	−0.4
Graphite average temperature (°C)	710.4	722.1	709.8	710.2	706.0	711.3
Max deviation from initial graphite average temperature (°C)	–	+11.7	−0.6	−1.9	−4.4	+0.9
Primary coolant temperature at IHX inlet (°C)	700.0	711.5	699.5	699.7	694.4	701.1
Max deviation from initial primary coolant temperature at IHX inlet (°C)	–	+11.5	−0.5	−0.34	−5.6	+1.1
Primary coolant temperature at IHX outlet (°C)	672.4	683.1	674.3	672.04	664.1	674.1
Max deviation from initial primary coolant temperature at IHX outlet (°C)	–	+10.7	+1.9	−0.4	−8.3	+1.8
Secondary coolant temperature at IHX inlet (°C)	610.1	622.3	613.4	612.5	591.8	613.7
Max deviation from initial secondary coolant temperature at IHX inlet (°C)	–	+12.2	+3.3	+2.4	−18.3	+3.6
Secondary coolant temperature at IHX outlet (°C)	630.2	642.8	633.7	630.8	614.1	633.4
Max deviation from initial secondary coolant temperature at IHX outlet (°C)	–	+12.6	+3.5	+0.6	−16.1	+3.2

Table 9 Response time (s) of FHER after inserting transient disturbance

Transient states	1	2	3	4	5
Power (MW)	–	5.5	22.5	40.0	60.0
P.C. at core inlet	68.0	23.0	23.0	30.0	168.0
P.C. at core outlet	5.5	1.0	40.0	46.0	183.0
S.C. at IHX inlet	30.5	25.0	0.8	1.0	41.0
S.C. at IHX outlet	22.0	11.5	0.5	8.0	48.0

P.C. primary coolant, *S.C.* secondary coolant

primary coolant in core inlet and outlet increase by 1.8 and 1.1 °C, respectively. The secondary coolant temperatures in IHX inlet and outlet increase by 3.6 and 3.2 °C, respectively. These results argue the necessity to control the variation range and rate of inlet temperature of air coolant.

3.3.6 Variations of FHER during transient disturbances

We summarize the simulation results above in Tables 8 and 9, so to analyze influence of the disturbance and to compare with other disturbances. In the first row of the tables, No. 1–5 represent the five transient states. The '+' and '−' signs denote the change direction of variables. The response time is the time period from the initial time of transient disturbances insertion to apparent change of target variable.

The transient of reactivity insertion affect FHER greatly. It increases the nuclear power sharply, while the coolant responds slowly in temperature, but the system can return to normal level benefited from the negative temperature reactivity feedback and large heat capacity. For other disturbed transients, the power and coolant curves barely change observably, and the heat transfer process of coolant in core and IHX is considerably slow. The results also indicate that the system possesses sufficient heat inertia and an abundant inherent self-stabilization to reach steady state, even with an insertion of disturbed transient.

4 Conclusion

OCFHR code is developed to analyze FHRs transient behaviors under normal operation. By comparing with other algorithm models and point reactor analytical solution, the results prove that the algorithm adopted in OCFHR is suitable for solving stiff equations. According to the five disturbed transient modes, the results fully verify the FHRs' inherent characteristics, such as high temperature, low pressure, and large heat capacity, negative reactivity coefficients, which result in slow response and unobvious variations during transient operation. For the reactivity step-inserted mode, the nuclear power changes promptly, while the temperature of molten salt responds quite slowly. The results indicate FHRs negative reactivity feedback plays a vital role to stabilize power. For the latter flow rate shifting modes, the power's responses to these changes have certain delays because of salt's large heat capacity and long circulation looping time. Besides, the IHX and SHX equipment can buffer rapid thermal dynamic impact and increase delay time, which can help to increase operator's response time. Concerning the power conversion unit, the fan model

adopted is not appropriate and a power cycle unit shall be developed for generation application.

The research of OCFHR is to complete the control and protection module for detailed FHR transient behaviors and suitable operation strategy.

References

1. C. Forsberg, The advanced high-temperature reactor: high-temperature fuel, liquid salt coolant, and liquid-metal reactor plant. Prog. Nucl. Energy **47**(1–4), 32–43 (2005). doi:10.1016/j.pnucene.2005.05.002
2. TMSR center, SINAP. Pre-conceptual Design of a 2 MW pebble bed fluoride salt coolant high temperature test reactor (2012)
3. D.F. Williams, Assessment of candidate molten salt coolants for the advanced high-temperature reactor (AHTR). ORNL-TM-2006-12 U.S. Department of energy (2006). doi:10.2172/885975
4. C.H. Andrades, A.T. Cisneros, J.K. Choi et al., Technical description of the "mark 1" pebble-bed fluoride-salt-cooled high-temperature reactor (PB-FHR) power plant. UCBTH-14-002. Department of Nuclear Engineering, University of California, Berkeley (2014). doi:10.13140/RG.2.1.4915.7524
5. M. Chen, I.H. Kim, X. Sun et al., Transient analysis of an FHR coupled to a helium Brayton power cycle. Prog. Nucl. Energy **83**, 283–293 (2015). doi:10.1016/j.pnucene.2015.02.015
6. M. Li, J. Zhang, Y. Zou et al., Disturbed transient analysis with stable operation mode of TMSR-SF1. NURETH-16, Hyatt Regency Chicago, America, August 30–September 4, on CD-ROM (2015). http://www.ans.org/store/item-700399/
7. Q. Lv, H.C. Lin, I.H. Kim et al., DRACS thermal performance evaluation for FHR. Annu. Nucl. Energy **77**, 115–128 (2015). doi:10.1016/j.anucene.2014.10.032
8. G. Ablay, A modeling and control approach to advanced nuclear power plants with gas turbines. Energy Convers. Manag. **76**, 899–909 (2013). doi:10.1016/j.enconman.2013.08.048
9. C. Forsberg, L.W. Hu, P. Peterson et al. Fluoride-salt-cooled high-temperature reactor (FHR) for power and process heat. MIT-ANP-TR-157 (2014)
10. X. Huang, Research of Runge–Kutta method. Heilongjiang Sci. Technol. **23**, 23–27 (2012). doi:10.3969/j.issn.1673-1328.2012.23.063. **(in Chinese)**
11. M.R. Galvin, *System Model of a Natural Circulation Integral Test Facility* (Oregon State University, Corvallis, 2009)
12. W. van Antwerpen, C.G. du Toit, P.G. Rousseau et al., A review of correlations to model the packing structure and effective thermal conductivity in packed beds of mono-sized spherical particles. Nucl. Eng. Des. **240**, 1803–1818 (2010). doi:10.1016/j.nucengdes.2010.03.009
13. N. Wakao, S. Kaguei, T. Funazki et al., Effect of fluid dispersion coefficients on particle-to-fluid heat transfer coefficients in packed beds. Chem. Eng. Sci. **34**, 325–336 (1978). doi:10.1016/0009-2509(79)85064-2
14. S. Ergun, Fluid flow through packed columns. AIChE J. **18**(2), 361–371 (1972)
15. S.S. Lomakin, Y.A. Nechaev, Transient processes and the measurement of reactivity of a reactor containing Beryllium. Translated from Atomnaya Energiya **18**(1), 33–40 (1965). doi:10.1007/BF01116353
16. S. Yang et al., *Heat Transfer* (Beijing Higher Education Press, Beijing, 2006), pp. 243–263
17. M. Lin, Y.Q. Chen, H. Zhang et al., Extension of RELAP5 core power calculation model. Nucl. Power Eng. **28**, 16–19 (2007). doi:10.3969/j.issn.0258-0926.2007.06.005. (**in Chinese**)